Received: 6 December 2022 | Revised: 6 April 2023 | Accepted: 29 April 2023

DOI: 10.1111/jace.19218

Journal of the American Ceramic Society

RESEARCH ARTICLE

Determination of the controlling parameters for dislocation nucleation in $SrTiO_3$: An investigation by nanoindentation

Xiaomei Wang[1,4] | **Xiaowei Liu**[2] | **Yingwei Li**[1,3,6] | **Xufei Fang**[5]

[1]School of Civil Engineering, Wuhan University, Wuhan, Hubei, China

[2]Shenzhen Institute of Advanced Electronic Materials, Shenzhen Institute of Advanced Technology, Chinese Academy of Sciences, Shenzhen, China

[3]Guangdong Provincial Key Laboratory of Functional Oxide Materials and Devices, Southern University of Science and Technology, Shenzhen, Guangdong, China

[4]Department of hydraulic Engineering, Hubei Water Resources Technical College, Wuhan, China

[5]Department of Materials and Earth Sciences, Technical University of Darmstadt, Darmstadt, Germany

[6]Technische Universität Darmstadt, Darmstadt, Germany

Correspondence
Yingwei Li, School of Civil Engineering, Wuhan University, 430072 Wuhan, Hubei, China.
Technische Universität Darmstadt, Karolinenpl. 5, 64289 Darmstadt, Germany.
Email: yingweili@whu.edu.cn

Xufei Fang, Department of Materials and Earth Sciences, Technical University of Darmstadt, 64287 Darmstadt, Germany.
Email: fang@ceramics.tu-darmstadt.de

Xiaomei Wang and Xiaowei Liu contribute equally to this work.

Xufei Fang, affiliated to Karlsruhe Institute of Technology since 2023.01, but the research activity is not related to this submission.

Editor's Choice
The Editor-in-Chief recommends this outstanding article.

Funding information
National Natural Science Foundation of China, Grant/Award Numbers: 11972262, 12272275; Guangdong Provincial Key Laboratory Program, Grant/Award Number: 2021B1212040001; Athene Young Investigator Programme at TU Darmstadt

[Correction added on 27 July 2023, after first online publication: Third affiliation to Yingwei Li was added.]

Abstract

We conduct nanoindentation to investigate dislocation nucleation in $SrTiO_3$ (STO) single crystals with surface orientations of (0 0 1), (0 1 1), and (1 1 1) with loading/unloading rates of 25, 250, and 2500 μN/s. Results reveal that the critical loads (P_c) at which "pop-in" event occurs depend strongly on surface orientations, but slightly related to loading rate. Based on P_c, the critical shear stress that triggers dislocation nucleation was determined by extracting the maximum resolved shear stress (τ_{max}) along the slip systems of STO using the Hertzian solution. The dislocation activation shear stress (τ_a) was determined by averaging τ_{max}. The determined τ_a is 9.0–12.0 GPa, close to the shear strength ($\sim G/2\pi$) of STO, indicating that homogeneous dislocation nucleation dominates the pop-in events. The consistency of the determined τ_a demonstrates that the frameworks for nanoindentation pop-in analysis established for metals can be extended to ceramics, whereas the influence of the limited slip systems should be taken into consideration. Additionally, we estimated the activation volume and the activation energy via the statistical model proposed by Schuh et al. The small values of the determined activation volume (0.6–9.8 Å^3) and the activation energy (0.13–0.70 eV) indicate that the dislocation nucleation possibly begins from a single-atom migration and local point defects may participate in the dislocation nucleation process. That is, heterogeneous nucleation may exist initially but the homogeneous dislocation nucleation dominates the pop-in events.

KEYWORDS
activation energy, activation volume, dislocation nucleation, nanoindentation pop-in, strontium titanate

1 | INTRODUCTION

Dislocations are line defects in crystalline solids. In metals, dislocations can multiply and move easily under stress with amplitude much smaller than their theoretical strength, thus their existence has significant impact on the mechanical properties of metals, for example, plasticity and fracture toughness.[1,2] In contract to metals, however, the motion of dislocation in ceramics is rather difficult due to the strong ionic and covalent bonds. Thus, at room temperature, much larger shear stress is normally required to drive dislocation motion in ceramics. Moreover, metals usually have a very high preexisting dislocation density, which is not the case for ceramics. These characteristics generally render dislocations irrelevant for mechanical properties of ceramics.[3] Therefore, the research on dislocation behavior in ceramics is far less advanced than that on metallic materials. After intensive efforts conducted in the 1960s and 1970s on revealing the dislocation geometry configuration and the influence of dislocation on the deformation behavior of ceramics, related investigations on dislocation behavior in ceramics at room temperature have basically stopped for a long time and only few works were published until renewed attention arose within the last 20 years, triggered by the work of Nakamura et al.[4] They reported that Ti can diffuse along dislocations in plastically deformed sapphire to form conducting nanowires, and they proposed that dislocations in ceramics can be used as a promising tool to tune the functional properties.

In fact, dislocations have long been known to significantly affect the functional properties of ceramics. As early as in 1961, Harrison[5] reported that dislocations could enhance the transportation of anion in alkali halides. Later, Döding and Labusch[6] found that the electronic conductivity of plastically deformed single crystalline CdS increases due to the existence of dislocations. Recently, inspired by the work of Nakamura et al., several researchers started to intentionally engineer dislocations into ceramics to tune the conductivity and other functional properties. For instance, Bishara et al.[7] reported that dislocation could enhance the electrical conductivity in rutile TiO_2 accessed by room-temperature nanoindentation. Hameed et al.[8] found that in plastically deformed strontium titanate, superconductivity and ferroelectric quantum criticality were significantly enhanced. Szot et al.[9–11] reported that in single crystals of a prototypical perovskite oxide $SrTiO_3$ (henceforth referred as STO) with naturally occurring dislocations, the materials provide bistable switching of the conductance between nonmetallic and metallic behaviors under an appropriate electric field. Oshima et al.[12] reported that the optical bandgap of plastically deformed ZnS was distinctly decreased after deformation, with reason arising from the smaller bandgap at the dislocation core. Höfling et al.[13] reported that the polarization of barium titanate crystal can be controlled by dislocations, due to the strong mechanical restoring force yielded by the microstructure formed during plastic deformation of the material, which reverts electric field-induced domain wall displacement on the macroscopic level and high pinning force on the local level. At present, it is becoming clear that dislocations (1-dimensional) could be developed as a new strategy to tune the functional properties of ceramics, with potentially more superior effect to the previously used methods, such as elements doping (0-dimensional), interface engineering (2-dimensional), and the second phase doping (3-dimensional).

In order to develop ceramics with required functionality for applications by dislocation engineering,[14] it is important that dislocation networks must be introduced into the materials first. Up to date, several technologies, such as flash-sintering,[15] protons irradiating,[16] defect chemistry engineering,[17] and mechanical loading,[18,19] have been reported. Among these approaches, mechanical loading is thought to be most promising due to the fact that the dislocation mesostructured as well as the density could be well controlled (confined on the slip planes) if the load is applied on ceramics in a controlled manner.[20] As demonstrated by Johanning et al.,[21] after uniaxial deformation of a STO single crystal in [1 0 0] direction with a pre-introduced notch, well-aligned dislocations with directions along $\{1\,1\,0\}\langle 0\,1\,1\rangle$ could be introduced in the materials.

In ceramics, the formation of dislocation networks was also accomplished by dislocation nucleation, multiplication, and motion under mechanical load, akin to metals.[14] However, unlike in metals, the density of dislocations in initially fabricated ceramics is normally much lower, for example, 1.8×10^{10} m^{-2} for STO single crystal. As the preexisting dislocations play a very important role in the plastic deformation behavior of ceramics, in order to introduce the desired dislocation networks in them, the physical processes of dislocation nucleation should be understood and the parameters that control this process should be determined. However, investigations on this topic are rather few, except a few publications on single-crystal STO,[22] MgO,[23] and TiO_2[7] by nanoindentation. In some of these analyses, the activation shear stress (τ_a) of ceramics was calculated based on the theoretical framework established from metals, for example, in the paper by Fang et al.,[17] by the equation of $\tau_a = 0.31(\frac{6E_r^2}{\pi^3 R^2}P_{pop-in})^{1/3}$. It is yet unknown whether the framework of metals can be directly transferred to ceramic research, as the number of slip systems of ceramics is significantly smaller than that of metals. Additionally, there are often some point defects such as oxygen vacancies and dopants in ceramic materials,

which has been reported to have influence on the dislocation nucleation and motion.[17,22] Previously, dislocation nucleation in ceramics studied by nanoindentation pop-in tests were mostly referred to be homogenous based on the calculated maximum shear stress.[24] Here, we provide quantitative analyses of the activation volume and the activation energy, which shed more lights on the dislocation nucleation process in ceramics. Our investigations demonstrate that to determine the dislocation mode, except the activation shear stress, the activation volume and the activation energy should also be determined and analyzed.

In this work, we conducted nanoindentation experiments in STO single crystals with different surface orientations of (0 0 1), (0 1 1), and (1 1 1) with loading and unloading rates of 25, 250, and 2500 μN/s. The corresponding dislocation τ_a was determined by extracting the maximum resolved shear stress (τ_{max}) in the direction along the slip systems of STO using the stress field beneath the indenter with Hertzian solution. We also estimated V and ε via the statistical model proposed by Schuh et al. The determined parameters of τ_a, V, and ε were used to discuss the effect of crystallographic directions on the observed orientation-dependent critical loads (P_c) at which the "pop-in" event occurs, and mechanisms that possibly have influence on the dislocation nucleation process.

Here, we choose STO crystal as the model material. On one hand, it is a prototypical perovskite oxide with cubic structure with six slip systems of $\langle 011\rangle\{110\}$ at room temperature,[25–29] and out of these six slip systems, only two are independent, due to the fact that some of the slip systems produce the same plastic strain. On the other hand, the ionic transport ability of STO by oxygen migration, which is the basis for their applications, such as electronic devices,[10,11] high-temperature electrochemical cells,[30] and oxygen sensors,[31] have been reported can be significantly influenced by dislocation, as oxygen vacancies possess a highly anisotropic elastic dipole tensor, which can provide a mechanism to shield local internal strains induced by dislocations. Moreover, the dislocation densities and distribution in STO can be easily characterized via chemical etching technique.[17,32,33]

2 | SAMPLE PREPARATION AND EXPERIMENTAL PROCEDURES

2.1 | Sample preparation

The STO single crystal, grown by the Verneuil technique, was provided by HF-Kejing Co., Ltd., Hefei, China. Three rectangular specimens, with a dimension of $5 \times 5 \times 1$ mm^3 and surface orientation (0 0 1), (0 1 1), and (1 1 1), were used. For all the samples, their two opposite 5×5 mm^2 surfaces were polished carefully by diamond paste, with a roughness of 5 nm. As polishing will introduce dislocations in STO, and the preexisting dislocation is supposed to influence the nanoindentation behavior, we etched the polished surfaces of specimens before nanoindentation test to clarify the density of the preexisting dislocation by an etchant (10 mL 65% HNO_3 with few drops of 40% HF).[34,35] The dislocation density calculated from characterization by scanning electron microscope (SEM) reveals that (Figure 1A–C) the dislocation density on the etched surface is about 1.8×10^{10} m^{-2}, with the dislocation spacing of nearest neighbor of about 3 μm. It indicates the corresponding statistical probability of 1% that the submicron sized indentation tip would contact the pre-dislocations in the indented area of 20 μm $\times$ 20 μm. Therefore, we can reasonably deduce that influence of the preexisting dislocations on the nanoindentation results can be excluded.[36] The X-diffraction characterization by the SIEMENS D5000 X-ray diffractometer equipped with Cu-K_α radiation was carried out to assure the surfaces of specimens to be tested in the exact orientations (Figure 1D), as conducted by Wu et al.[37] Furthermore, by using energy-dispersive spectroscopy we characterized the elements of the specimen and the results revealed that Ca, Ba, and Mg existed in the materials with concentrations in regime of 30–200 at ppm.

2.2 | Experimental procedures

Nanoindentation tests were conducted at room temperature using the Hysitron Ti 950 TriboIndenter system (Hysitron Inc., Minneapolis, MN, USA) with a diamond Berkovich indenter. Before indentation experiments, the Berkovich tip geometry and area function was calibrated using fused quartz while the tip radius was fitted using the Hertzian elastic contact.[35] The determined tip radius of the indenter is ~200 nm. Considering the tip radius of around 200 nm and the first pop-in events happened at about 20 nm, before the pop-in events, the Berkovich tip can be assumed as spherical, that is, the calibration process used here is valid.[35] Additionally, according to previous investigations,[38,39] the first pop-in events observed at depth of ~20 nm during nanoindentation can be assumed to be dominated by dislocation nucleation and motion without cracks. During testing, load-controlled mode was applied with three loading rates of 25, 250, and 2500 μN/s to the maximum load of 5 mN. For each specimen in a given loading condition, a matrix of 7×8 grid nanoindentations were performed with 20 μm interval apart from each other (Figure 2A) to ensure that any overlap of plastic zones and dislocation structure created by neighboring indentations can be avoided.[36]

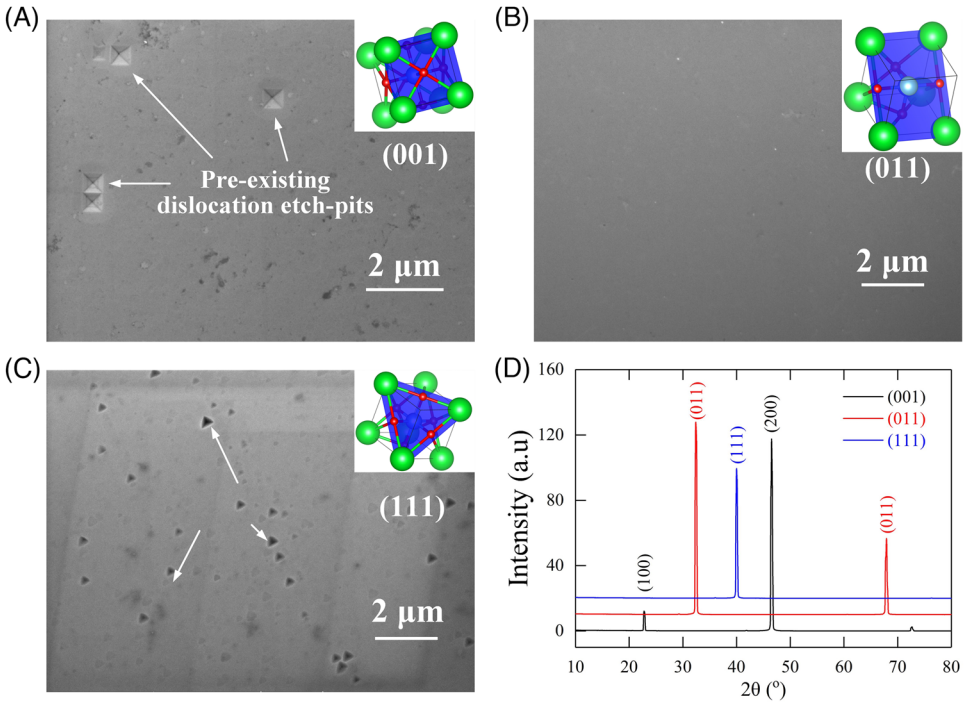

FIGURE 1 (A–C) Scanning electron microscopy (SEM) images of etched pits on the surface of the sample give an averaged dislocation density of about 1.8×10^{10} m^{-2}. Inserts are illustration of the crystallographic structure of specimen. (D) X-ray diffractometer (XRD) spectrum of STO specimens.

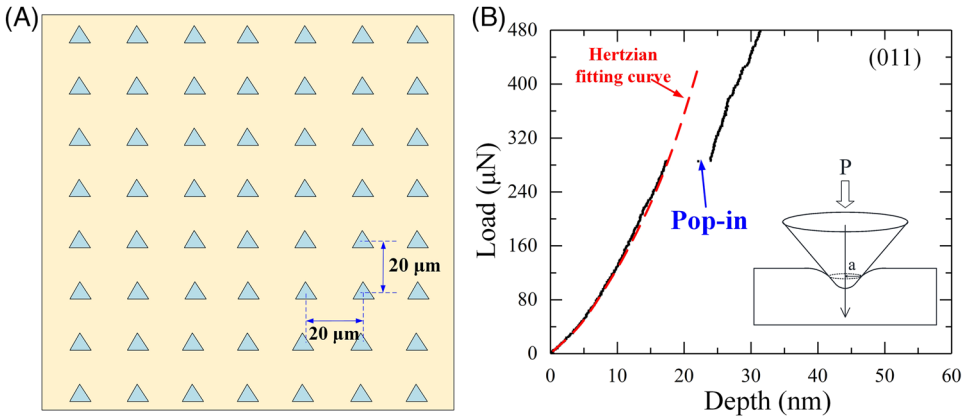

FIGURE 2 (A) Schematic diagram of nanoindentation experiments. (B) Representative nanoindentation load–displacement curve measured on (011) surface of STO single crystal.

Figure 2B displays a typical load–displacement (P–h) curve measured on the (011) STO single crystal with the loading rate of 250 μN/s. When the applied load reach to a critical value, the P–h curve exhibits a typical displacement burst (indicated as pop-in), which is generally raised from the dislocation nucleation and motion. Considering the preexisting dislocation density in the pristine STO is rather low ($\sim 1.8 \times 10^{10}$ m^{-2}), the pop-in can be assumed to occur in a dislocation-free region.[2] On the other hand, the pop-in events always happened shallower than 100 nm promises spherical surface contacts at the depth probed in the present study.[40] Thus prior to pop-in event, the measured P–h curves can be well described by the Hertzian elastic relation[41]:

$$P = \frac{4}{3} E_r \sqrt{R} h^{3/2} \tag{1}$$

where h is the penetration displacement measured from the sample surface down to the bottom of the contact, R is the effective tip radius of 200 nm, and E_r is the reduced

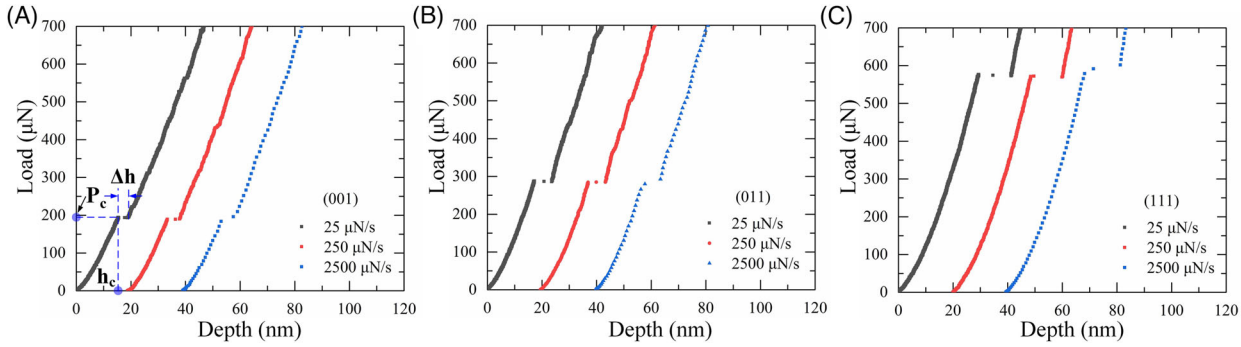

FIGURE 3 Representative load–depth curves measured on (A) (0 0 1)-oriented surface; (B) (0 1 1)-oriented surface; and (C) (1 1 1)-oriented surface with loading rates of 25, 250, and 2500 μN/s, respectively.

elastic modulus determined by the elastic deformation occurring in both the specimen and the indenter, deduced by

$$\frac{1}{E_r} = \frac{1-\upsilon_i^2}{E_i} + \frac{1-\upsilon_s^2}{E_s} \tag{2}$$

with $E_i = 1140$ GPa and $\upsilon_i = 0.07$ for the Young's modulus and the Poisson's ratio of the diamond tip, E_s and $\upsilon_s = 0.237$ for the Young's modulus and the Poisson's ratio of STO.[42] The Hertzian fitting curves are shown in Figure 2B in red dotted line. The overlap of the measured and the predicted curves demonstrates that prior to the pop-in, the interaction between the indenter and the sample is elastic.

2.3 | Characterizations of dislocations using SEM after chemical etching

Details of the generated dislocations and the corresponding distributions in the tested specimens were characterized by SEM. All the samples were etched with the same etchant (10 mL 65% HNO_3 with few drops of 40% HF) for 20 s after the indentation to reveal the dislocation configurations. Both the surface morphology and etch-pit features around the nanoscale residual impressions of STO were characterized by SEM (Zeiss Sigma 500, Germany) with an acceleration voltage of 10 kV.[17]

3 | RESULTS

3.1 | Pop-in events under different loading rates

Figure 3A–C displays the representative load–depth curves of the (0 0 1), (0 1 1), and (1 1 1) STO single crystals at different loading rates. We denote the pop-in load as P_c, the corresponding burst depth as Δh, and the depth for the onset of pop-in as h_c, as depicted in Figure 3A. In all 504 nanoindentation points of the three crystallographic orientations specimen, there are only 12 data points without detectable pop-in events. From all the nanoindentation curves, we identified that the critical loads (P_c) at which the "pop-in" event occurs depend strongly on the crystallographic orientations, but only slightly related to the loading rates.

Detailed, statistical analysis of the distribution of P_c and Δh for all valid nanoindentation results with pop-in events is summarized in Figure 4A,B, respectively. On (0 0 1) surface, the average values of P_c at loading rate of 25, 250, and 2500 μN/s are 161.50, 169.99, and 168.79 μN, respectively. Correspondingly, the average values of Δh are 3.20, 3.46, and 4.15 nm. On (0 1 1) surface, the average values of P_c at the same loading rates as that of (0 0 1) surface are 276.48, 292.33, and 303.50 μN, with corresponding values Δh of 5.30, 5.81, and 6.88 nm. A much higher average pop-in load on (1 1 1) surface is observed, with the average values of P_c of 548.89, 567.51, 598.82 μN, and the corresponding values of Δh are 11.01, 11.35, and 12.81 nm.

In Figure 4C, we plotted P_c versus Δh and observed that the data points fall on almost straight line regardless of the surface orientations. Such a phenomenon is similar to that of single crystalline aluminum and copper as reported in literature,[43] which can be explained by the load-amplitude depended on motion of the dislocations after nucleation. That is, under larger load, the dislocations can move longer.

Figure 5 plots the relationship between the pairs of P_c and $h_c^{1.5}$ of the total 492 nanoindentation points for each specimen. The linear relationship verifies that for all the measured load–depth curves, the deformation behavior of STO was dominated by elastic behavior before the occurrence of pop-in event.[41] According to $P = \frac{4}{3}E_r\sqrt{R}h^{1.5}$, the reduced modulus E_r can be deduced by $E_r = \frac{3\beta}{4\sqrt{R}}$. Here, β represents the slope of the $P_c - h_c^{1.5}$ data, which can be determined by fitting the experiment data in Figure 5.

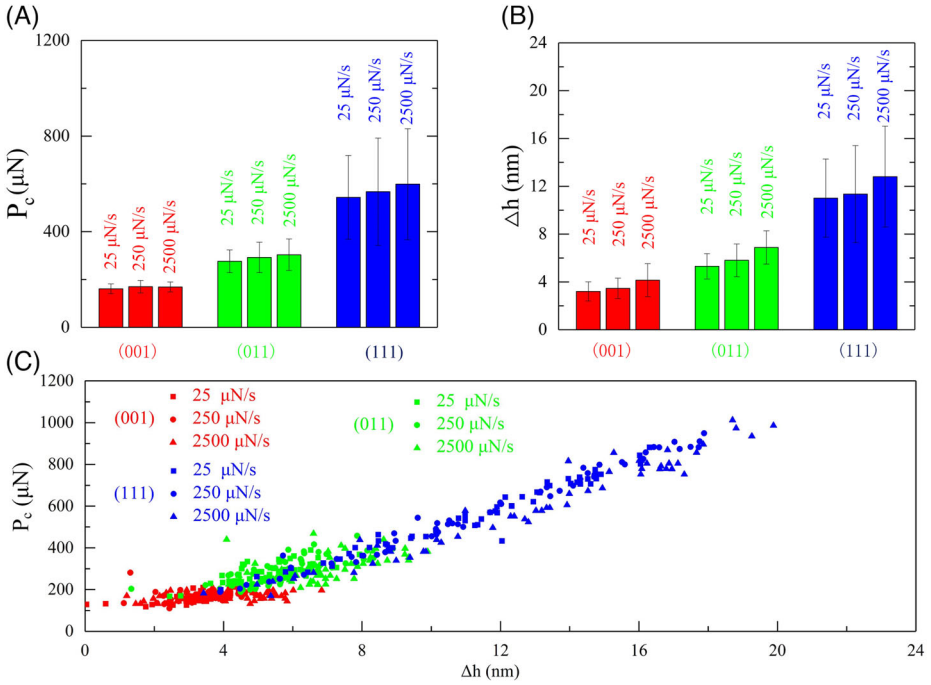

FIGURE 4 (A) The averaged pop-in load P_c, (B) the averaged burst depth Δh, and (C) the relationship between P_c and Δh on the (0 0 1), (0 1 1), and (1 1 1) STO single crystals with different loading rates.

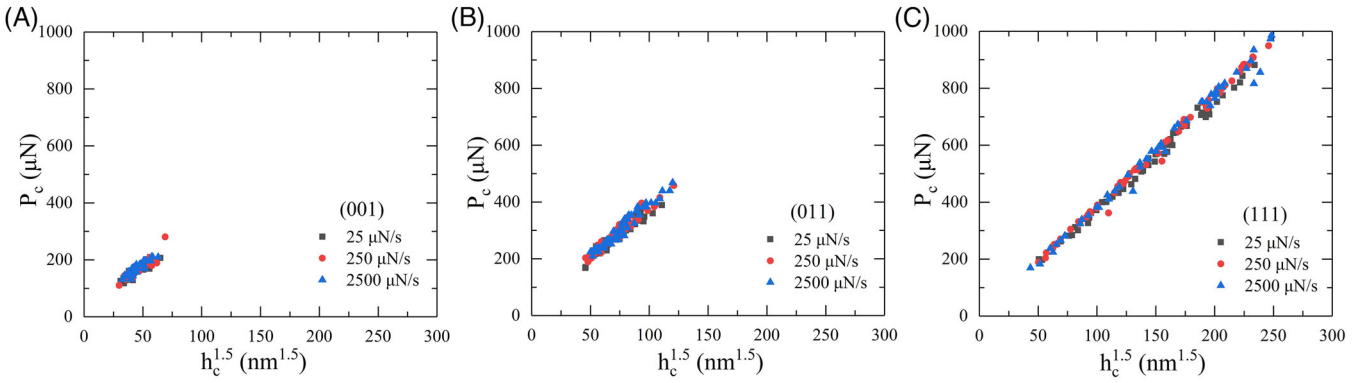

FIGURE 5 The statistics of P_c versus $h_c^{1.5}$ at pop-in measured on samples with different surface orientations: (A) (0 0 1), (B) (0 1 1), and (C) (1 1 1) at different loading rates which follow a linear correlation upon Hertzian contact theory.

The obtained experiment data and the calculated E_r were summarized in Table 1. Noted that the obtained reduced moduli E_r (~200 GPa) was slightly smaller than the values of 224 GPa compared with the values from Ref. [14] reported previously, which was possibly caused by the difference of the used materials.

3.2 | SEM images of three different STO crystals surface

As there is little dependence of pop-in load on the loading rates, here, Figure 6 only presents the SEM images of the dislocation etch-pits with a loading rate of 25 μN/s. On (0 0 1) surface (Figure 6A), the dislocation pile-ups are aligned in ⟨1 0 0⟩ and ⟨0 1 1⟩ directions and exhibit an eight-armed intersecting quadratic feature with an angle of about 45°, which agrees with the results reported by Yang et al.[44] and Javaid et al.[32] On (1 1 1) surface, around the indentation imprint there are six arms along ⟨1_ 1_ 2_⟩ directions, possessing a threefold symmetry (Figure 6C). In addition, the dislocation arms on the indented (1 1 1) surface are longer than the other two surface orientations, indicating an easier expansion of the plastic zone.

However, on (0 1 1) plane (Figure 6B), no visible dislocation etch pits were observed, which may be due to the fact that the surface itself is a slip plane.[45] At room temperature, plasticity of STO single crystals is accounted

TABLE 1 Summary of the depth (h_c) and load (P_c) for the first pop-in measured from different planes at different loading rates.

Indented plane	Loading rate (μN/s)	Load P_c (μN)	Depth h_c (nm)	Burst depth Δh (nm)	Reduced modulus E_r (GPa)	Fitting constant β (μN/nm$^{3/2}$)
(0 0 1)	25	161.50 ± 21.28	12.58 ± 1.31	3.20 ± 0.80	204.06 ± 11.78	3.56 ± 0.03
	250	169.99 ± 26.02	12.74 ± 1.48	3.46 ± 0.85	211.01 ± 10.85	3.70 ± 0.03
	2500	168.79 ± 20.91	12.55 ± 1.23	4.15 ± 1.38	216.30 ± 11.49	3.76 ± 0.03
(0 1 1)	25	276.48 ± 47.52	17.04 ± 2.29	5.30 ± 1.06	215.68 ± 10.71	3.87 ± 0.03
	250	292.33 ± 63.72	17.39 ± 2.83	5.81 ± 1.37	219.77 ± 10.84	3.96 ± 0.03
	2500	303.50 ± 65.96	17.76 ± 2.76	6.88 ± 1.39	225.07 ± 10.42	4.00 ± 0.03
(1 1 1)	25	548.89 ± 176.62	27.41 ± 6.02	11.01 ± 3.27	198.25 ± 5.11	3.74 ± 0.01
	250	567.51 ± 224.25	27.39 ± 7.38	11.35 ± 4.06	205.32 ± 4.06	3.86 ± 0.01
	2500	598.82 ± 231.97	28.37 ± 7.62	12.81 ± 4.22	207.13 ± 4.13	3.87 ± 0.02

Note: The fitting constant β, the reduced modulus (E_r) are also listed for comparison.

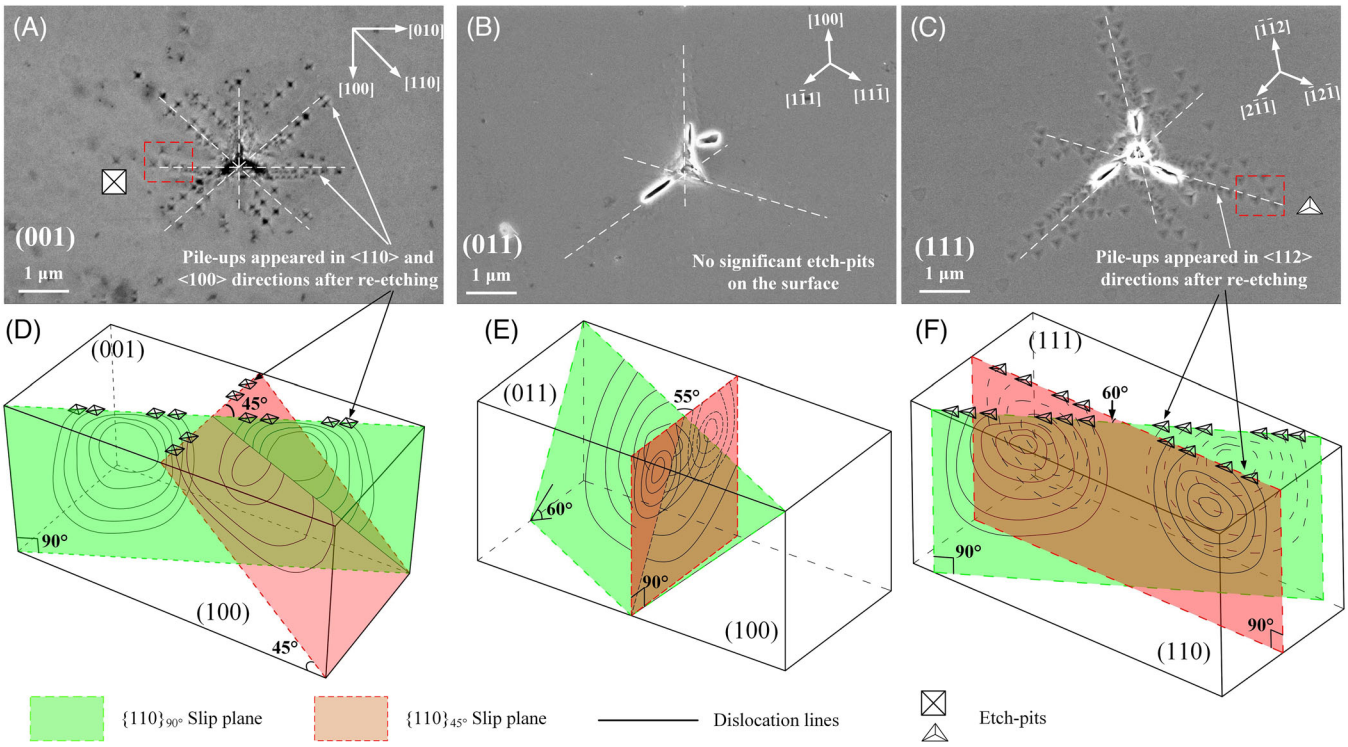

FIGURE 6 Scanning electron microscopy (SEM) images of etched STO samples after indentation tests: (A) (0 0 1), (B) (0 1 1), and (C) (1 1 1) with the same loading rate of 25 μN/s. (D–F) Schematic illustrations of the corresponding slip systems and dislocation structure.

for by {1 1 0}⟨0 1 1⟩ slip systems with six equivalent slip planes.[26,27,29] Two of the six slip planes are perpendicular to the (0 0 1) plane (denoted as $\{110\}_{90°}$ in green square), and the other four are inclined at 45° from the (0 0 1) plane (denoted as $\{110\}_{45°}$ in red square). From the shape of etch pits and the reported results of Javaid et al.,[33] further insight into the three-dimensional distribution of the dislocations construction can be obtained. On the (0 0 1)-indented surface, etch pits in the ⟨0 1 1⟩ and ⟨0 0 1⟩ directions suggest that the dislocation pile-ups lie on $\{110\}_{90°}$ and $\{110\}_{45°}$, respectively. However, on (0 1 1) plane, the slip plane should be (1_1 0), which is oriented to the indented surface at 90° and the rest of four slip planes inclined at 60° to the indented surface. On (1 1 1) plane, both the slip planes of $\{110\}_{90°}$ and $\{110\}_{45°}$ are perpendicular to the (1 1 1) surface and intersect the indentation plane along ⟨1 1 2⟩ directions and ⟨1 0 1⟩ directions. There must be 12 arms of etch pits, 6 lie along ⟨1_1_2_⟩, and the other 6 lie along ⟨1_0 1⟩. As revealed by the chemical etching technique and 3D dislocation structure analysis from Javaid et al.[33] on (0 0 1) surface of STO, the schematic representation of the dislocation half loops around the residual impressions in STO with various crystal orientations is shown in Figure 6D,E.

4 | DISCUSSIONS

4.1 | Estimating the activation shear stress

For STO crystal, the dislocation nucleation stress is intrinsic and thus independent of crystal orientation. Thus, in STO, the resolved shear stress with direction along its slip systems should be taken into account.[46,47] In the following, the "Easy-slip" model[48] was adopted to quantify the orientation dependence of the critical resolved shear stress (τ_{CRSS}) for the specific slip systems of {1 1 0}⟨0 1 1⟩ in STO.

For dislocations gliding on $\{110\}_{45°}$ and $\{110\}_{90°}$ slip planes, the stress field was generated by an elastic sphere–plane contact, which was first established by Hertz.[41] Due to the assumed rotational symmetry of nanoindentation and the internal symmetry properties of the cubic STO lattice, the relevant inclined angles (Φ) between indented plane and slipping planes are 45° and 90° for (0 0 1) orientation, 60° and 90° for (0 1 1) orientation, and 90° for (1 1 1) orientation, respectively, as schematically illustrated in Figure 6D–F.

The nonzero components of stress tensor of the Hertzian stress field in cylindrical coordinates (r, φ, z) are σ_{rr}, $\sigma_{\varphi\varphi}$, σ_{zz}, and τ_{rz}. When the indenter is applied on the sample with P_c, τ_{CRSS} on the {1 1 0}⟨0 1 1⟩ slipping system are determined according to the following equation[49,50]:

$$\tau_{CRSS} = n_r^c v_r^c \sigma_{rr} + n_\varphi^c v_\varphi^c \sigma_{\varphi\varphi} + n_z^c v_z^c \sigma_{zz} + (n_r^c v_z^c + n_z^c v_r^c)\tau_{rz} \quad (3)$$

$$\tau_{\max} = \max\{\tau_{CRSS}\} = S_{mid} P_m \quad (4)$$

where n_i^c and v_i^c denote the i-th component of the slip plane normal and slip direction of the slip system, respectively; P_m the maximum contact pressure; S_{mid} is the so-called indentation Schmid-factor-ratio of the maximum resolved shear stress (τ_{max}) to the maximum contact pressure.[50] The calculated contour plots of τ_{CRSS}/P_m for the {1 1 0}⟨0 1 1⟩ slip system are indicated for different inclined angles determined by crystal orientations in Figure 7. Considering the repetition of the inclined angles between slip plane and crystallographic indented planes, here we only present the contour maps of the inclined angles of 45°, 60°, and 90°. It is clear that crystal orientation has a significant influence on the localized τ_{max} via S_{mid}. The values of S_{mid} are 0.2938, 0.2926, and 0.2135 for Φ = 45°, 60°, and 90°, respectively. It is important to note that, when Φ = 45° and 60°, τ_{max} often locate at the point below the surface, at a position located about 0.5r (r is the contact radius) along the indent axis, which is consistent with the work reported by Swain and Lawn.[38,51] When Φ = 90°, it is at a position approximately 0.5r directly below the contact circle.

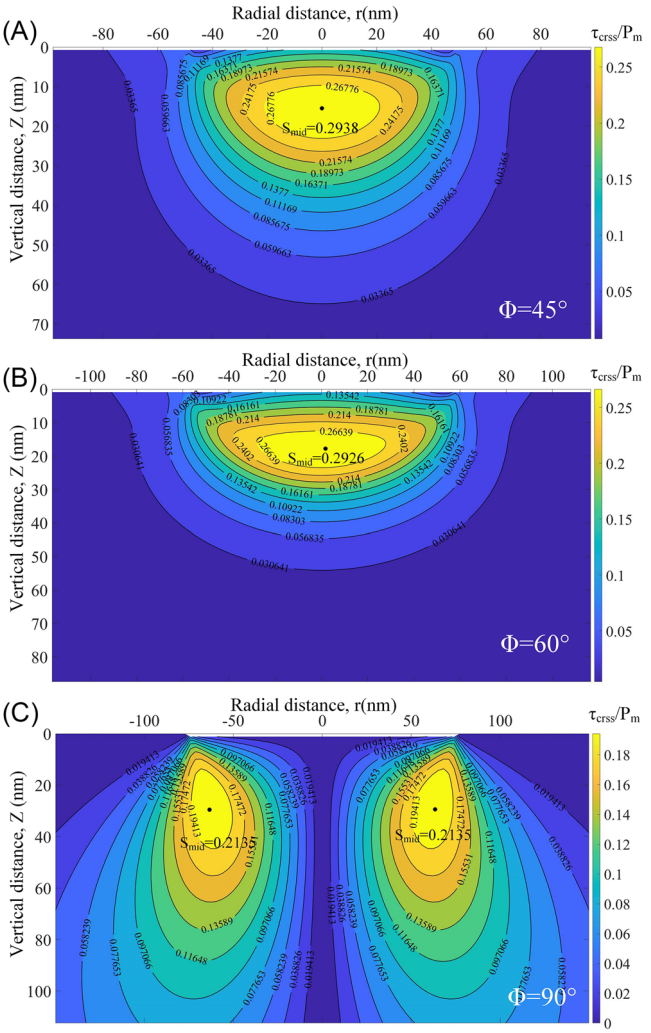

FIGURE 7 Contour plots of τ_{CRSS}/P_m on the {1 1 0}⟨0 1 1⟩ slip systems at the critical load of pop-in events calculated for different crystallographic orientations in STO: (A) Φ = 45° for (0 0 1)-indented plane; (B) Φ = 60° for (0 1 1)-indented plane; and (C) Φ = 90° for (1 1 1)-indented plane. In both orientations, the calculated plots correspond to that slip system of the {1 1 0}⟨0 1 1⟩ slip systems at the inclined angles between slip plane and crystallographic indented planes of STO crystal which inclined angles between slip plane and crystallographic indented planes.

In Equation (3), the maximum contact pressure $P_m = (\frac{6E_r^2 P_c}{\pi^3 R^2})^{1/3}$, and the corresponding contact radius r is given by[41]:

$$r = \left(\frac{4\gamma P_c R}{3E_S}\right)^{1/3} \quad (5)$$

where, R is the radius of the indenter, E_s is the Young's modulus of the STO, and γ is a factor given by:

$$\gamma = \frac{9}{16}\left[\left(1-\upsilon_i^2\right) + \left(1-\upsilon_s^2\right)\frac{E_s}{E_i}\right] \quad (6)$$

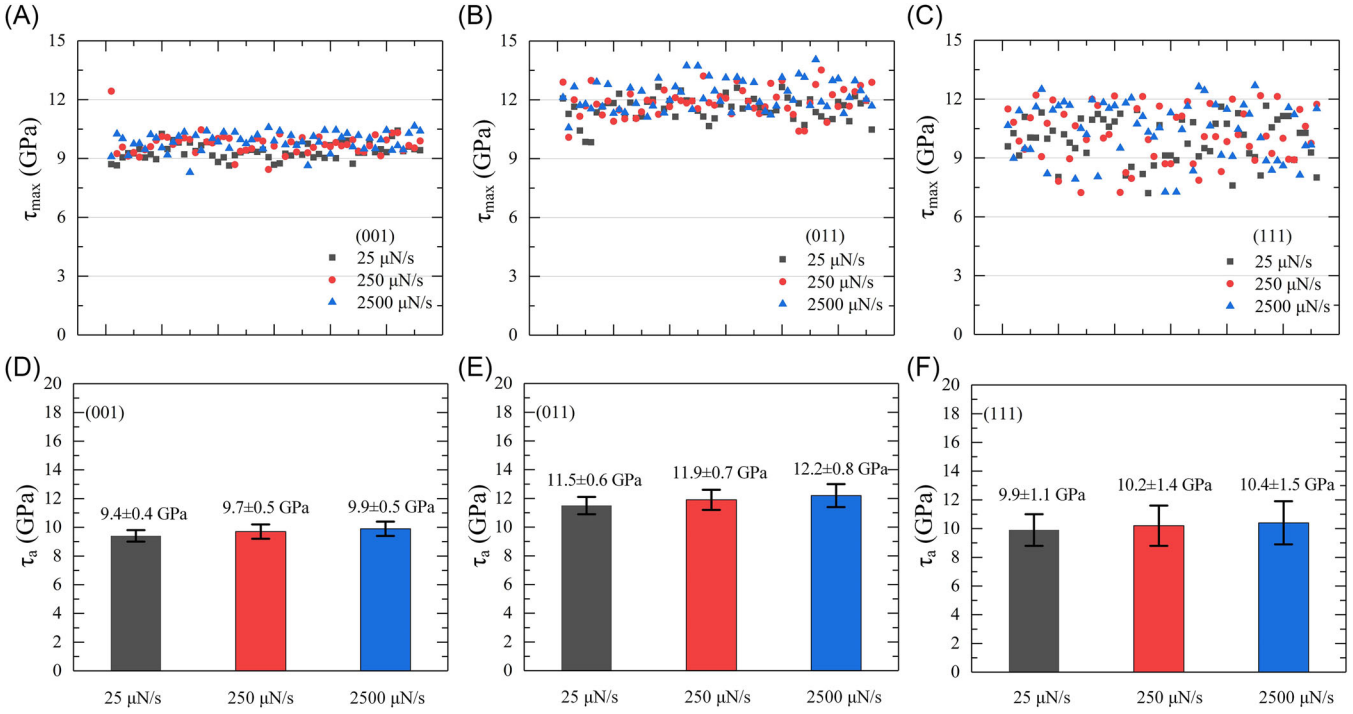

FIGURE 8 The determined maximum resolved shear stress τ_{max} from P_c obtained at the pop-in events (492 date points) on different nanoindentation planes: (A) (0 0 1), (B) (0 1 1), and (C) (1 1 1), and the corresponding average values τ_a: (D) (0 0 1), (E) (0 1 1), and (F) (1 1 1), respectively. All the values are roughly equivalent irrespective of orientation and fall into the range of theoretical strength (G/14–G/7).

In Figure 8, we plotted the determined maximum resolved shear stress τ_{max} and their average values τ_a. The phenomenon that all the maximum shear stress is roughly equivalent irrespective of orientation is consistent with the results by Taeri et al.[27] On (0 0 1) surface with loading rates of 25, 250, and 2500 μN/s, the determined τ_a are 9.4 ± 0.4, 9.7 ± 0.5, and 9.9 ± 0.5 GPa, respectively; on (0 1 1) surface, the determined τ_a are 11.5 ± 0.6, 11.9 ± 0.7, and 12.2 ± 0.8 GPa; on (1 1 1) surface, the determined τ_a are 9.9 ± 1.1, 10.2 ± 1.4, and 10.4 ± 1.5 GPa. The consistency of the determined τ_a demonstrates that the dislocation gliding on the unitary slip system should account for the approximate shear stress irrespective of the loading direction. Moreover, all the τ_a are in the range of 8.0–13.0 GPa, close to the estimated theoretical strength ($\sim G/2\pi$), with $G = \frac{E}{2(1+\upsilon)}$ being the shear modulus of the related orientation (98.37, 103.99, and 94.45 GPa for (0 0 1), (0 1 1), and (1 1 1), respectively).

Based on the critical resolved shear stress criteria, one would favor dislocation initiation to occur at the point of τ_{max}. For (0 0 1)-indented surface, activation of dislocations initiates at sites close to $\{1\,1\,0\}_{45°}$ planes below the center of the contact, followed by the $\{1\,1\,0\}_{90°}$ planes. Interestingly, the lengths of ⟨0 1 1⟩ dislocation pile-up exceed those of ⟨1 0 0⟩ pile-up (Figure 6), which suggests that edge dislocation gliding in the ⟨0 1 1⟩ pile-up is easier compared to the screw dislocations in the ⟨1 0 0⟩ directions. The dominating dislocation types in these different directions have been suggested by Javaid et al.[32] For (0 1 1)-indented surface, τ_{max} appears in the $\{1\,1\,0\}_{90°}$ planes, with 60° inclined to the surface of the contact circle.

4.2 | Estimating the dislocation activation parameters from statistic modeling

Here, we adopt the stress-biased nucleation model proposed by Schuh et al.[52,53] to characterize the time dependent nucleation of dislocations and quantitatively compare the nucleation mechanism on crystals with different orientations. Due to the probabilistic nature of the atomic-level events beneath the indenter, nucleation-based incipient plasticity, which is also a thermally activated process, is analyzed statistically. Values of the η, V, and ε of incipient plasticity were extracted to allow for direct comparison in different loading rates and crystal orientations.

Statistically, the probability of nucleation-based events per unit volume can be described in the form[38,53,54]:

$$\dot{n} = \eta \cdot \exp\left(-\frac{\varepsilon - \sigma V}{kT}\right) \tag{7}$$

where η is the attempt frequency; kT is the thermal energy equal to Boltzmann's constant k multiplied by temperature T; ε is the intrinsic nucleation energy barrier (activation enthalpy); and σ is the stress over the activation volume V.

By integrating over the volume near the contact region (Ω) beneath the indenter, the global rate ($\dot{N}$) at which displacement bursts would occur can be found[53]:

$$\dot{N} = \eta \cdot \exp\left(-\frac{\varepsilon}{kT}\right) \cdot \iiint_{\Omega} \exp\left(\frac{\sigma V}{kT}\right) d\Omega \tag{8}$$

The change rate of cumulative fraction function, $F(t)$ is inversely correlated with the number of remaining unyielded samples, and to the rate at which one of those remaining samples displays the onset of plasticity $\dot{F}(t) = [1 - F(t)]\dot{N}(t)$. Then, the cumulative statistics that we obtain from experimentation are easily connected to the rate equation as[37,52,53]

$$F(t) = 1 - \exp\left(-\int_0^t \dot{N}\left(t'\right) dt'\right) \tag{9}$$

where t is time, for a constant loading rate $\dot{P}$, we can obtain $t = P_c / \dot{P}$, and the integral runs from the beginning of the indentation to the current time under consideration.

Here we take the assumption that $\sigma = \tau_{\max} = S_{mid}(\frac{6PE_r^2}{\pi^3 R^2})^{1/3}$ because the displacement burst corresponds to the nucleation occurring primarily due to the action of the shear stress, τ. and $\Omega \approx Kr^3 = K(\frac{4\gamma P_c R}{3E_c})$, where K is proportionality constant which we take to be $\sim\pi$.[53]

Then the cumulative fraction function can be written as

$$F(P) = 1 - \exp\left\{-\frac{9KR\eta}{4E_r\dot{P}\alpha^6}\exp\left(-\frac{\varepsilon}{kT}\right)\begin{bmatrix}120 + \exp\left(P_c^{1/3}\alpha\right)\cdot\left(P_c^{5/3}\alpha^5 - 5P_c^{4/3}\alpha^4 + 20P_c\alpha^3\right.\\ \left.-60P_c^{2/3}\alpha^2 + 120P_c^{1/3}\alpha - 120\right)\end{bmatrix}\right\} \tag{10}$$

Here the parameter α is a collection of time-independent terms and is given by

$$\alpha \equiv S_{mid}\left(\frac{E_r^2}{\pi^2 R^2}\right)^{1/3}\frac{V}{kT} \tag{11}$$

The statistically cumulative distribution for the first pop-in load is graphically represented in Figure 9 (dotted line). We treat all the three parameters of η, V, and ε as adjustable and fit Equation (10) to the experimental data. The solid green lines in Figure 9 are the fitting results. These graphs demonstrate the proper sigmoidal trend of the curves captured in our statistical interpretation of incipient plasticity and the loading rate independence in the cumulative distributions, with the coefficient of determination $R^2 > 0.97$.

The determined parameters of ε and V are listed in Table 2, which all decrease with the increase of the averaged P_c for different STO crystals. The largest activation volume was obtained on (0 0 1)-oriented STO, with the values of 8.2–9.8 Å^3. The smallest values of 0.4–1.2 Å^3 were obtained on (1 1 1)-oriented STO. Intermediate values of 2.6–4.8 Å^3 were evaluated in (0 1 1)-oriented STO. For ε, the determined values are 0.51–0.70, 0.23–0.50, and 0.13–0.29 eV for STO with surface orientation of (0 0 1), (0 1 1), and (1 1 1), respectively. This means that as the increase of the stress under the indenter (larger P_c means larger stress field), the dislocation nucleation becomes easier.

In the frame of homogeneous dislocation nucleation, the pop-in event involves a cooperative motion of atoms to form a critical-sized dislocation loop, in which the motion of multiatomic and the breaking of multiatomic bonds involved. Hence, the activation energy would be on the order of several eV.[40,52] Considering that the lattice constant (c) of STO is ~3.905 Å and the corresponding atomic volume is c^3,[54] and that the values of the determined V are all smaller than the volume of one atomic, it can be concluded that point-like substance was participated in the dislocation nucleation process. This scenario is similar to the arguments derived by Stich et al. on the (0 0 1)-oriented STO,[22] Dong et al. on the GaN single crystals,[55] Qiu et al. on KDP single crystal,[56] and Ma et al. on $LiTaO_3$ single crystal.[57] That is, the dislocation nucleation is possibly determined by the quantity and mobility of mobile dislocation sources.[54,58] For instance, for STO single crystal, the activation energies of oxygen vacancies are 0.62–1.2 eV, and the activation energies of the other intrinsic defects are larger than 1 eV.[30] This means that oxygen vacancy sites could work as one type of dislocation source.

Note that the values of the determined τ_a are in the range of ~G/14 to ~G/7, close to the theoretical strength of STO. Consequently, similar to the arguments given by,[59] from the determined data of τ_a, ε, and V by nanoindentation for STO, it can be deduced that during loading, heterogeneous nucleation may exist initially, but the pop-in events were dominated by homogeneous dislocation nucleation.

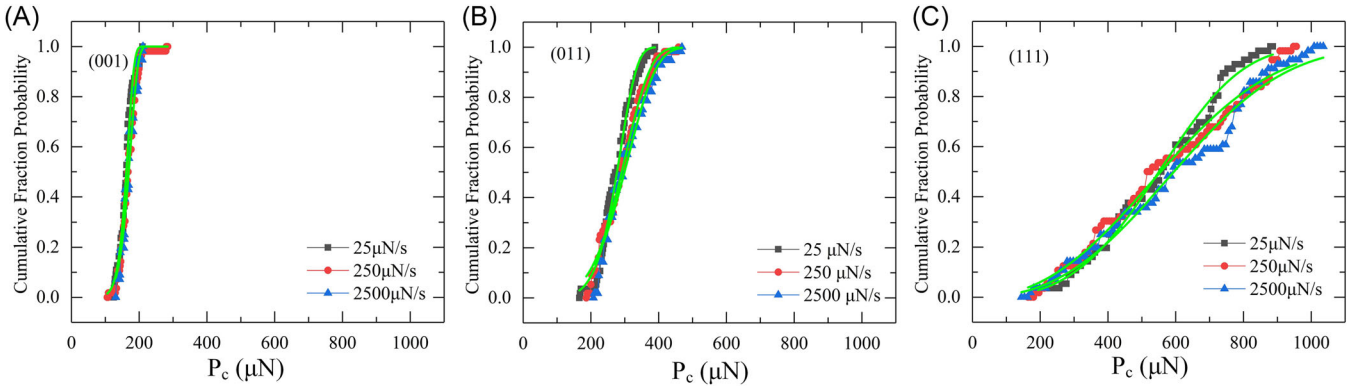

FIGURE 9 The cumulative distribution of P_c with different loading rate for three crystal orientations: (A) (0 0 1), (B) (0 1 1), and (C) (1 1 1), which is of weak loading rate dependence. The experimental datasets (shown as points) are well captured by the statistics of thermal activation through Equations (10), as illustrated by the solid green lines.

TABLE 2 The estimated activation energy (ε) and the activation volume (V) in single-crystal STO with different surface orientations and different loading rates.

Indented plane	Loading rate (μN/s)	Activation volume V (Å^3)	α	Activation energy ε (eV)	R^2
(0 0 1)	25	9.8	430.4	0.6986	0.9827
	250	8.3	372.5	0.5693	0.9961
	2500	8.2	372.5	0.5086	0.9762
(0 1 1)	25	4.8	218.8	0.4967	0.9888
	250	3	136.1	0.3114	0.9917
	2500	2.6	121.4	0.231	0.9758
(1 1 1)	25	1.2	50.49	0.2906	0.9919
	250	0.4	17.83	0.1691	0.987
	2500	0.6	25.75	0.1289	0.9838

5 | CONCLUSION

In this work, the dislocation nucleation process in single-crystal STO was studied by nanoindentation pop-in tests on (0 0 1), (0 1 1), and (1 1 1) surface orientations with various loading rates of 25, 250, and 2500 μN/s. The main conclusions are summarized as follows:

1. There exist distinctive pop-in loads among different crystal orientations for single-crystal STO but the loading rate dependence for pop-in load is negligible.
2. Based on Hertz theory and the "Easy-slip" model, shear strength in STO single crystal was calculated in the range of 8.0–13.0 GPa, which is roughly consistent with each other for all the three orientations and close to the estimated theoretical strength ($\sim G/2\pi$). Additionally, the consistency of the determined τ_a from the three representative crystallographic orientations demonstrates that the frameworks established for nanoindentation pop-in analysis in metals can be extended to ceramics, whereas the influence of the slip systems of ceramics should be taken into consideration.
3. Using a nucleation-based statistical framework, we obtained quantitative controlling parameters of V (0.6–9.8 Å^3) and ε (0.13–0.70 eV), indicating that the dislocation nucleation possibly begins from a point-like substance and oxygen vacancy sites could work as one type of dislocation nucleation source. From the determined data of τ_a, ε, and V by nanoindentation for STO, it can be deduced that during loading, heterogeneous nucleation may exist initially, but the pop-in events were dominated by homogeneous dislocation nucleation. That is, to determine the dislocation mode in oxide ceramics, the V and ε should also be determined and analyzed.

ACKNOWLEDGMENTS

Y. Li acknowledge the support from the National Natural Science Foundation of China (Grant numbers 11972262,

12272275), and the Guangdong Provincial Key Laboratory Program (grant number 2021B1212040001). X. Fang acknowledges the financial support of the Athene Young Investigator Programme at TU Darmstadt.

Open access funding enabled and organized by Projekt DEAL.

ORCID

Yingwei Li https://orcid.org/0000-0002-8217-5511
Xufei Fang https://orcid.org/0000-0002-3887-0111

REFERENCES

1. Hirth JP, Lothe J. Theory of dislocations. Malabar, FL: Krieger publishing company; 1992.
2. Hull D, Bacon DJ. Introduction to dislocations. 5th ed. Oxford: Butterworth-Heinemann, Elsevier; 2011.
3. Meyers MA, Chawla KK. Mechanical Behavior of Materials 2nd ed. Cambridge: Cambridge university press; 1987.
4. Nakamura A, Matsunaga K, Tohma J, Yamamoto T, Ikuhara Y. Conducting nanowires in insulating ceramics. Nat Mater. 2003;2:453–6.
5. Harrison LG. Influence of dislocations on diffusion kinetics in solids with particular reference to the alkali halides. Trans Faraday Soc. 1961;57:1191–9.
6. Döding G, Labusch R. Anisotropic conductivity of CdS after plastic deformation and conduction along dislocations: II. Measurements on a microscopic scale. Phys Status Solidi (a). 1981;68:469–76.
7. Bishara H, Tsybenko H, Nandy S, Muhammad QK, Frömling T, Fang X, et al. Dislocation-enhanced electrical conductivity in rutile TiO_2 accessed by room-temperature nanoindentation. Scr Mater. 2022;212:114543.
8. Hameed S, Pelc D, Anderson ZW, Klein A, Spieker RJ, Yue L, et al. Enhanced superconductivity and ferroelectric quantum criticality in plastically deformed strontium titanate. Nat Mater. 2022;21:54–61.
9. Szot K, Speier W, Carius R, Zastrow U, Beyer W. Localized metallic conductivity and self-healing during thermal reduction of $SrTiO_3$. Phys Rev Lett. 2002;88:075508.
10. Szot K, Speier W, Bihlmayer G, Waser R. Switching the electrical resistance of individual dislocations in single-crystalline $SrTiO_3$. Nat Mater. 2006;5:312–20.
11. Szot K, Dittmann R, Speier W, Waser R. Nanoscale resistive switching in $SrTiO_3$ thin films. Phys Status Solidi (RRL) – Rapid Research Letters. 2007;1:R86–8.
12. Oshima Y, Nakamura A, Matsunaga K. Extraordinary plasticity of an inorganic semiconductor in darkness. Science. 2018;360:772–4.
13. Höfling M, Zhou X, Riemer LM, Bruder E, Liu B, Zhou L, et al. Control of polarization in bulk ferroelectrics by mechanical dislocation imprint. Science. 2021;372(6545):961–4
14. Fang X, Porz L, Ding K, Nakamura A. Bridging the gap between bulk compression and indentation test on room-temperature plasticity in oxides: case study on $SrTiO_3$. Crystals. 2020;10:933
15. Yang B, Shang Z, Li J, Phuah XL, Cho J, Wang H, et al. Effects of electric field on microstructure evolution and defect formation in flash-sintered TiO_2. J Eur Ceram Soc. 2022;42:6040–7.
16. Khafizov M, Pakarinen J, He L, Hurley DH. Impact of irradiation induced dislocation loops on thermal conductivity in ceramics. J Am Ceram Soc. 2019;102(12):7533–42.
17. Fang X, Ding K, Janocha S, Minnert C, Rheinheimer W, Frömling T, et al. Nanoscale to microscale reversal in room-temperature plasticity in $SrTiO_3$ by tuning defect concentration. Scr Mater. 2020;188:228–32.
18. Ma Y, Cao L, Hang W, Zhang T, Yuan J. Crystallographic orientation effect on the incipient plasticity and its stochastic behavior of a sapphire single crystal by spherical nanoindentation. Ceram Int. 2020;46:15554–64.
19. Amodeo J, Merkel S, Tromas C, Carrez P, Korte-Kerzel S, Cordier P, et al. Dislocations and plastic deformation in MgO crystals: a review. Crystals. 2018;8:240.
20. Okafor C, Ding K, Zhou X, Durst K, Rödel J, Fang X. Mechanical tailoring of dislocation densities in $SrTiO_3$ at room temperature. J Am Ceram Soc. 2021;105(4):2399–402.
21. Johanning M, Porz L, Dong J, Nakamura A, Li JF, Rödel J. Influence of dislocations on thermal conductivity of strontium titanate. Appl Phys Lett. 2020;117(2):021902.
22. Stich S, Ding K, Muhammad QK, Porz L, Minnert C, Rheinheimer W, et al. Room-temperature dislocation plasticity in $SrTiO_3$ tuned by defect chemistry. J Am Ceram Soc. 2022;105(2):1318–29.
23. Gaillard Y, Tromas C, Woirgard J. Quantitative analysis of dislocation pile-ups nucleated during nanoindentation in MgO. Acta Mater. 2006;54(5):1409–17.
24. Montagne A, Audurier V, Tromas C. Influence of pre-existing dislocations on the pop-in phenomenon during nanoindentation in MgO. Acta Mater. 2013;61:4778–86.
25. Brunner D, Taeri-Baghbadrani S, Sigle W, Rühle M. Surprising results of a study on the plasticity in strontium titanate. J Am Ceram Soc. 2001;84(5):1161–3.
26. Gumbsch P, Taeri-Baghbadrani S, Brunner D, Sigle W, Ruhle M. Plasticity and an inverse brittle-to-ductile transition in strontium titanate. Phys Rev Lett. 2001;87:085505.
27. Taeri S, Brunner D, Sigle W, Rühle M. Deformation behaviour of strontium titanate between room temperature and 1800 K under ambient pressure. Z Metallkd. 2004;95(6):433–46.
28. Brunner D. Low-temperature plasticity and flow-stress behaviour of strontium titanate single crystals. Acta Mater. 2006;54(19):4999–5011.
29. Sigle W, Sarbu C, Brunner D, Rühle M. Dislocations in plastically deformed $SrTiO_3$. Philos Mag. 2006;86(29–31):4809–21.
30. Hanzig J, Zschornak M, Mehner E, Hanzig F, Münchgesang W, Leisegang T, et al. The anisotropy of oxygen vacancy migration in SrTiO3. J Phys Condens Matter. 2016;28:225001.
31. Menesklou W, Schreiner HJ, Härdtl KH, Ivers-Tiffée E. High temperature oxygen sensors based on doped $SrTiO_3$. Sens Actuators, B. 1999;59(2–3):184–9.
32. Javaid F, Stukowski A, Durst K. 3D dislocation structure evolution in strontium titanate: Spherical indentation experiments and MD simulations. J Am Ceram Soc. 2017;100:1134–45.
33. Javaid F, Bruder E, Durst K. Indentation size effect and dislocation structure evolution in (001) oriented $SrTiO_3$ Berkovich indentations: HR-EBSD and etch-pit analysis. Acta Mater. 2017;139:1–10.

34. Lorenz D, Zeckzer A, Hilpert U, Grau P, Johansen H, Leipner HS. Pop-in effect as homogeneous nucleation of dislocations during nanoindentation. Phys Rev B. 2003;67(17):2101.
35. Bei H, Lu ZP, George EP. Theoretical strength and the onset of plasticity in bulk metallic glasses investigated by nanoindentation with a spherical indenter. Phys Rev Lett. 2004;93(12):125504.
36. Li J, Dehm G, Kirchlechner C. How close can indents be placed without risking an erroneous pop-in statistics? Materialia. 2019;7:100378.
37. Wu D, Nieh GT. Incipient plasticity and dislocation nucleation in body-centered cubic chromium. Mater Sci Eng A. 2014;609:110–5.
38. Lawn BR. Indentation of ceramics with spheres: a century after hertz. J Am Ceram Soc. 2005;81(8):1977–94.
39. Fang X, Bishara H, Ding K, Tsybenko H, Porz L, Höfling M, et al. Nanoindentation pop-in in oxides at room temperature: dislocation activation or crack formation? J Am Ceram Soc. 2021;104(9):4728–41.
40. Schuh CA, Lund AC. Application of nucleation theory to the rate dependence of incipient plasticity during nanoindentation. J Mater Res. 2004;19(7):2152–8.
41. Johnson KL. Contact mechanics. Cambridge, London: Cambridge University Press; 1985.
42. Gervais F. Strontium titanate ($SrTiO_3$). In: Handbook of optical constants of solids. Academic Press; 1997. p. 1035–47.
43. Shibutani Y, Tsuru T, Koyama A. Nanoplastic deformation of nanoindentation: crystallographic dependence of displacement bursts. Acta Mater. 2007;55(5):1813–22.
44. Yang KH, Ho NJ, Lu HY. Deformation microstructure in (001) single crystal strontium titanate by Vickers indentation. J Am Ceram Soc. 2009;92(10):2345–53.
45. Groenou AB Van, Kadijk SE. Slip patterns made by sphere indentations on single crystal MnZn ferrite. Acta Metall. 1989;37(10):2613–24.
46. Louapre D, Breder K. Hertzian indentation stress field equations. Int J Appl Ceram Technol. 2015;12(5):1071–9.
47. Csanádi T, Bl'anda M, Chinh NQ, Hvizdoš P, Dusza J. Orientation-dependent hardness and nanoindentation-induced deformation mechanisms of WC crystals. Acta Mater. 2015;83:397–407.
48. Csanádi T, Kovalčíková A, Dusza J, Fahrenholtz WG, Hilmas G.E. Slip activation controlled nanohardness anisotropy of ZrB_2 ceramic grains. Acta Mater. 2017;140:452–64.
49. Zhang W, Gao Y, Xia Y, Bei H. Indentation Schmid factor and incipient plasticity by nanoindentation pop-in tests in hexagonal close-packed single crystals. Acta Mater. 2017;134:53–65.
50. Li TL, Gao YF, Bei H, George EP. Indentation Schmid factor and orientation dependence of nanoindentation pop-in behavior of NiAl single crystals. J Mech Phys Solids. 2011;59(6):1147–62.
51. Swain MV, Lawn BR. A Study of Dislocation Arrays at Spherical Indentations in LiF as a Function of Indentation Stress and Strain. Phys Status Solidi (b). 1969;35(2):909–23.
52. Schuh CA, Mason JK, Lund AC. Quantitative insight into dislocation nucleation from high-temperature nanoindentation experiments. Nat Mater. 2005;4:617–21.
53. Mason JK, Lund AC, Schuh CA. Determining the activation energy and volume for the onset of plasticity during nanoindentation. Phys Rev B. 2006;73:054102.
54. Wollenberger HJ. Point defects. In: Physical metallurgy (Fourth Edition). Cahn RW, Hassen P, eds., North-Holland, Amsterdam, 1996; 1621-1721.
55. Dong Z, Zhang X, Peng S, Jin F, Wan Q, Xue J, et al. Mechanical properties of GaN single crystals upon C ion irradiation: nanoindentation Analysis. Materials. 2022;15:1210.
56. Qiu W, Wang X, Chen H, Hang W, Ma Y. Probing the stochastic behavior of the onset of plasticity for potassium dihydrogen phosphate single crystal by grating spherical nanoindentation. Ceram Int. 2022;48:28374–81.
57. Ma Y, Huang X, Hang W, Liu M, Song Y, Yuan J, et al. Nanoindentation size effect on stochastic behavior of incipient plasticity in a $LiTaO_3$ single crystal. Eng Fract Mech. 2020;226:106877.
58. Nakamura R, Masuda H, Yoshida H. Nanoindentation responses near single grain boundaries in oxide ceramics. J Am Ceram Soc. 2023;106:2061–72.
59. Gan K, Yan D, Zhu S, Li Z. Interstitial effects on the incipient plasticity and dislocation behavior of a metastable high-entropy alloy: nanoindentation experiments and statistical modeling. Acta Mater. 2021;206:116633.

How to cite this article: Wang X, Liu X, Li Y, Fang X. Determination of the controlling parameters for dislocation nucleation in $SrTiO_3$: An investigation by nanoindentation. J Am Ceram Soc. 2023;106:6085–6097.
https://doi.org/10.1111/jace.19218